Supporting Information:

Cryogenic single-molecule fluorescence annotations for electron tomography reveal in situ organization of key proteins in *Caulobacter*

Peter D. Dahlberg[1], Saumya Saurabh[2], Annina M. Sartor[1], Jiarui Wang[1,2], Patrick G. Mitchell[3], Wah Chiu[3,4], Lucy Shapiro[2], W.E. Moerner[1]

[1]Department of Chemistry, Stanford University, Stanford, California 94305, United States

[2]Department of Developmental Biology, Stanford University School of Medicine, Stanford, California 94305, United States

[3]Division of CryoEM and Bioimaging, Stanford Synchrotron Radiation Lightsource, SLAC National Accelerator Laboratory, Menlo Park, California 94025, United States

[4]Department of Bioengineering, Stanford University, Stanford, California 94305, United States

Email: wmoerner@stanford.edu

www.pnas.org/cgi/doi/10.1073/pnas.2001849117

Supplementary Figures

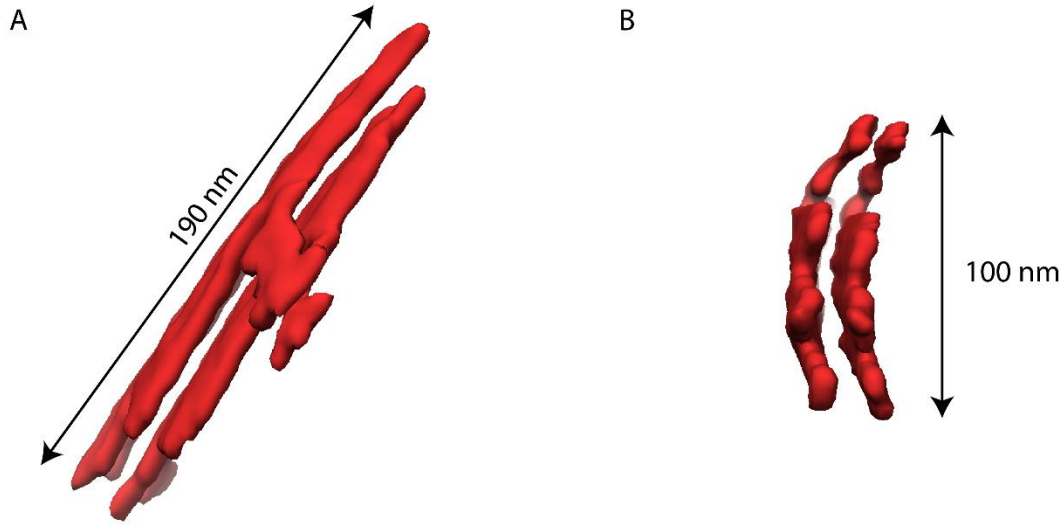

Figure S1: Manual annotation of the chemoreceptor array shown in Figure 1A. (A) Chemoreceptor array viewed from the top (same orientation as in Figure 1A). (B) Same array as in A, but rotated to look down the length of the array. The curve of the array along the inner membrane is apparent in this orientation.

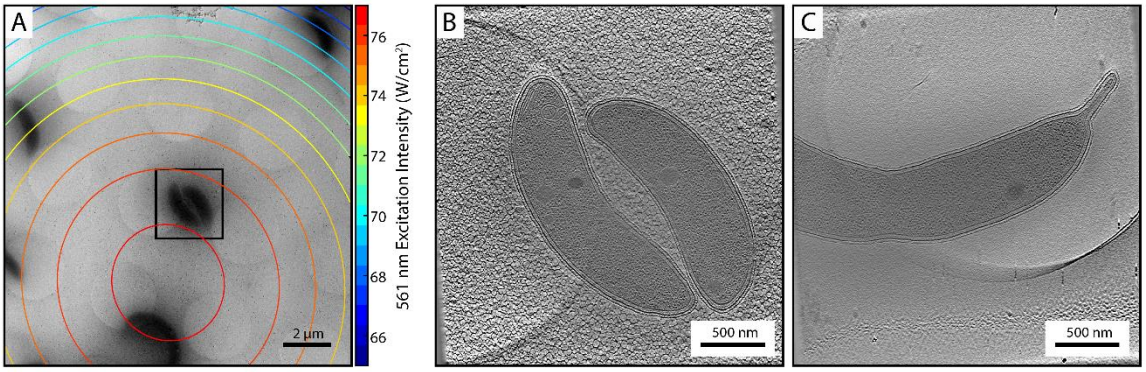

Figure S2: Optical excitation can cause devitrification even at low intensities. (A) Low magnification EM image with contours showing excitation intensity. (B) Tomographic slice of the cells outlined by the black box in A. Devitrified ice surrounding the cells is due to 2 hours and 45 minutes of fluorescence imaging. (C) Tomographic slice of a cell in the same grid square as B, but outside the range of fluorescence excitation, showing no devitrification. The rate of devitrification and the intensity at which it is observed is likely strongly dependent on ice thickness. Thicker ice can dissipate heat more rapidly without absorbing additional energy.

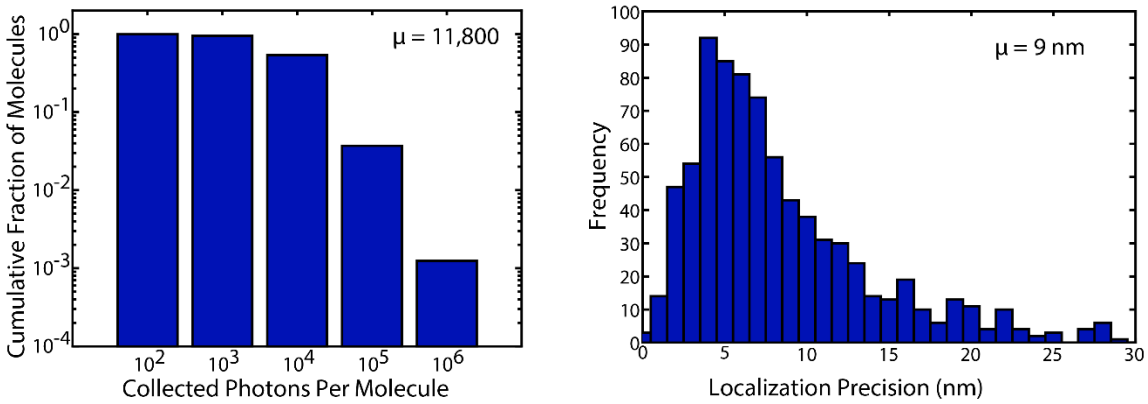

Figure S3: Merged emitter statistics for cryogenic localizations. (*Left*) Distribution of collected photons per emitter after merging localizations. (*Right*) Histogram of lateral localization precision for merged PAmKate emitters. The resulting average localization precision is 9 nm and 30% of localizations have precisions better than 5 nm.

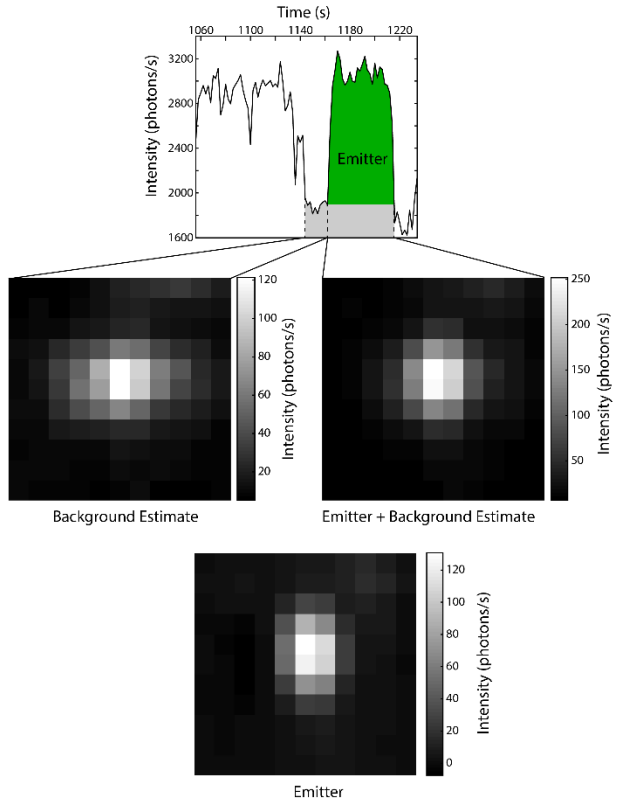

Figure S4: Background estimation and removal process. Top plot shows zoom-in of the intensity trace shown in Figure 3B. The background is estimated as the average frame corresponding to the time window outlined by the dashed lines. This background is then subtracted from the frames for which the emitter, highlighted in green, is present. This results in the PSF for the emitter alone, shown at the bottom, which is used for localization.

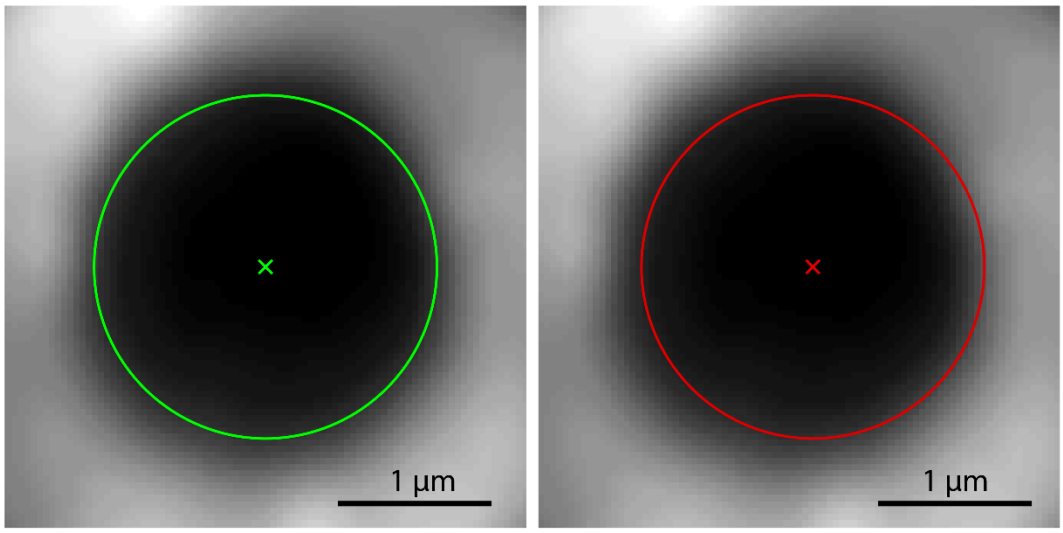

Figure S5: Example of a centered hole from the registration process. The green circle on the left is centered well on the image of the hole from the expanded average fluorescence data. The red circle on the right is overlaid on the same hole but is shifted 100 nm to the right. The shift is readily apparent and indicates the ability of the registration process to manually identify each individual hole center to better than 100 nm. While the precision with which an individual hole center can be identified is worse than the localization precision of a bright fluorescent bead, the large number of hole centers (typically 12-16) neighboring a cell of interest that can identified and used as control point pairs allows for a reduction in the overall registration error well below 100 nm, see Notes S1 and S2 and Figure S6.

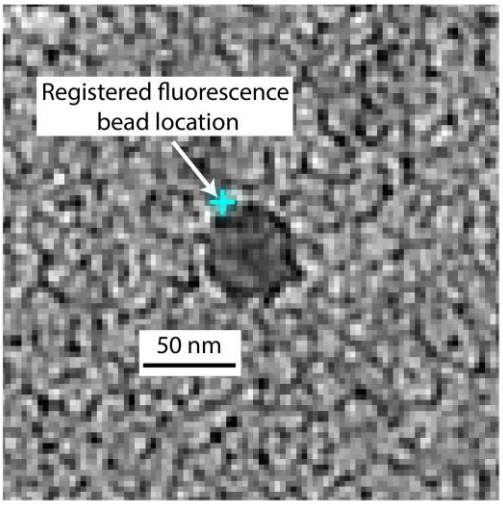

Figure S6: Results of the correlative workflow being applied to a tomogram of a 40 nm fluorescent polystyrene bead. The cyan cross marks the localization of the bead from fluorescence. The resulting shift of the fluorescence localization relative to the bead is ~30 nm and is dominated by the lateral registration error between the fluorescence data and the low magnification electron micrograph.

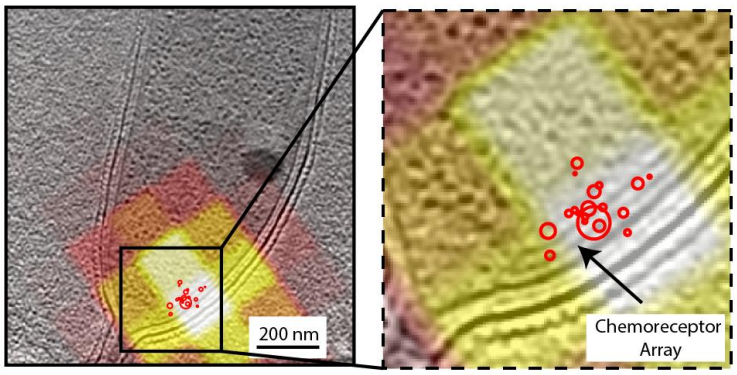

Figure S7: Same data as in Figure 4C with the addition of the diffraction-limited average fluorescence data shown as the overlaid heat map pixelated image.

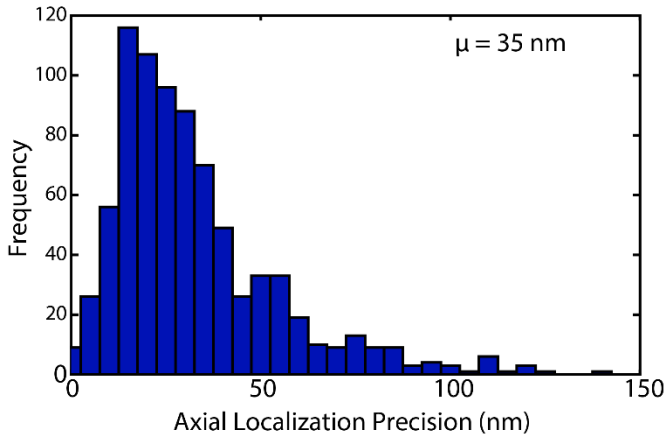

Figure S8: Histogram of axial localization precision. The axial localization precision is approximately two times worse than expected from the lateral localization precision due to errors induced by overlapping emitters.

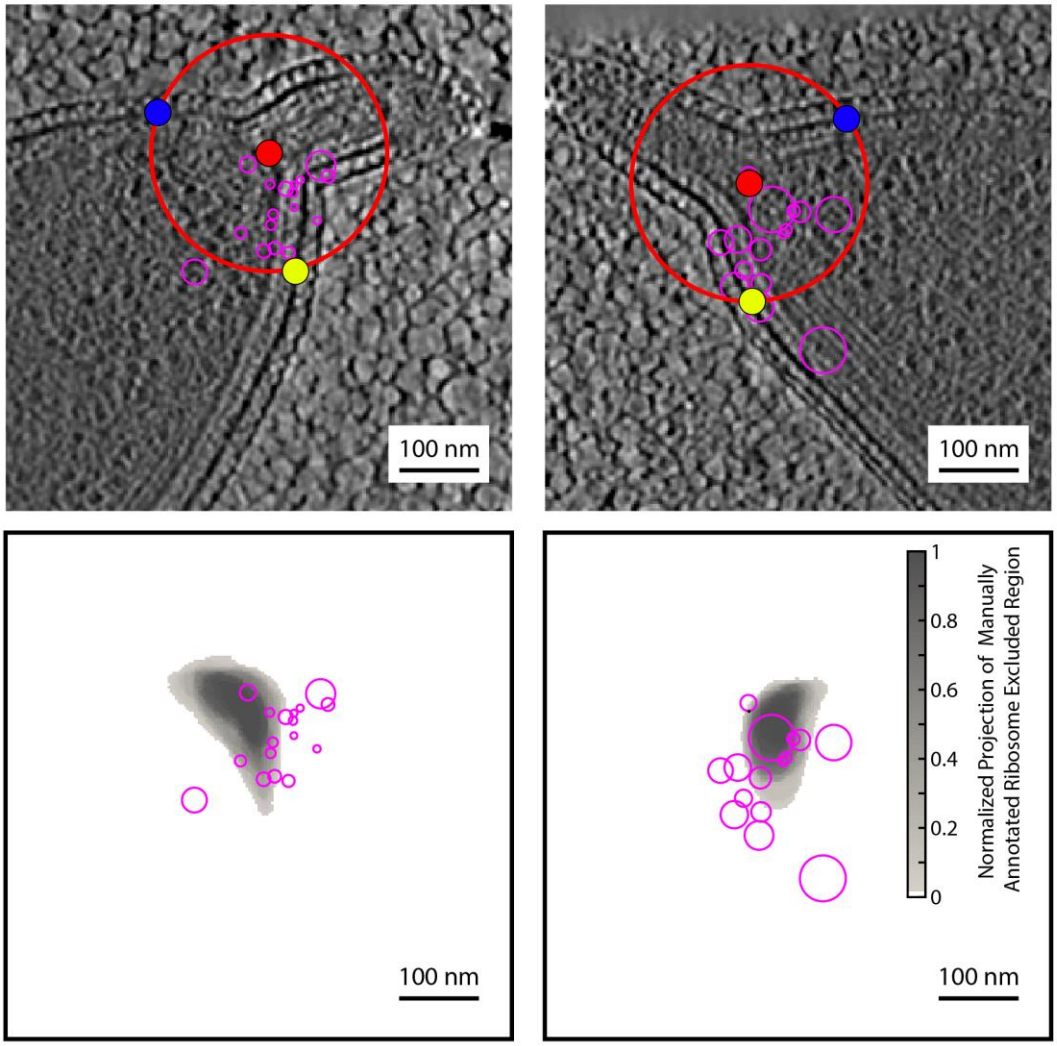

Figure S9: *Top panel:* Alignment markers for two cells expressing SpmX-PAmKate and used for the pooled localizations shown in Figure 6. The central red dot is placed manually at the base of the stalk. The blue and yellow circles are placed on the outer membrane where it crosses the red circle, which is ~300 nm in diameter and centered on the red dot. For SpmX labeled cells, like those shown here, the yellow circle was always placed on the side with the SpmX. The three markers are aligned only through reflection, translation, and rotation; there was no scaling adjustment to account for the slight differences between cell pole sizes. The cell shown on the left is the same as the cell shown in Figure 6A. *Bottom panel:* Same cells as shown above. Here, the SpmX localizations are visualized alongside the context of the manually annotated ribosome excluded region for each cell projected into the xy-plane. The closely matched spatial extent of SpmX and the ribosome excluded region is apparent for individual cells.

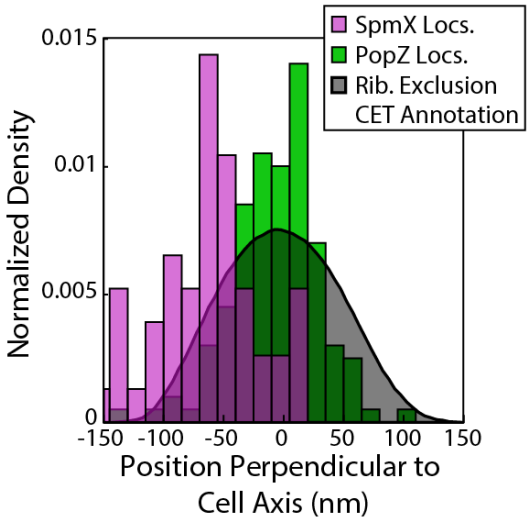

Figure S10: Distributions of SpmX and PopZ localizations perpendicular to the cell axis, where zero is defined as the middle of the stalk. The shaded gray curve is the result of manual annotation of the ribosome exclusion region from the CET data corresponding to the PAmKate-PopZ localizations.

Supplementary Notes

SI note 1: Projective image transformation using hole centers as control points

Many image registration techniques depend on selecting control point pairs. These control points are points that can be identified in two different images. Registered images are images that minimize the distance between control point pairs for a given image transformation. All image transformations to align the fluorescence microscopy data to the electron tomogram were tried using Matlab's fit geometric transformation function, "fitgeotrans". These transformations included the similarity, affine, projective, polynomial, piecewise linear, and local weighted mean transformations. In our experience, the projective transformation provided the most accurate and robust image registration. The projective transformation, as the name implies, is the transformation that projects points in one plane to another arbitrarily oriented plane. It is described using homogeneous coordinates by the following 3x3 matrix.

$$\begin{bmatrix} s_x & sh_y & t_x \\ sh_x & s_y & t_y \\ E & F & 1 \end{bmatrix}$$

Where s_x and s_y describe the scaling, sh_x and sh_y describe shear, t_x and t_y describe translation and E and F describe the vanishing point of the projection. These eight free parameters necessitate at least four control point pairs for a unique transformation matrix. The transformation carries points from the fluorescence microscopy image (x, y) to the electron microscopy space (x', y') through the following operation.

$$\begin{bmatrix} x' \\ y' \\ 1 \end{bmatrix} \cong \begin{bmatrix} wx' \\ wy' \\ w \end{bmatrix} = \begin{bmatrix} s_x & sh_y & t_x \\ sh_x & s_y & t_y \\ E & F & 1 \end{bmatrix} \begin{bmatrix} x \\ y \\ 1 \end{bmatrix}$$

For the application of registering fluorescence and electron microscopy images, we would ideally have as many precisely known control points as possible as close to a cell of interest as

possible. While large (~200 nm) fluorescent beads could be used as control points, it is challenging to achieve a high enough local density of beads (at least four close to a cell of interest) to provide accurate registration, but not so many as to obscure the underlying fluorescent imaging target. The regular pattern of holes in holey carbon grids provide a promising alternative to fluorescent beads for image registration due to their guaranteed high density of control points (~ 6 in a 10 x 10-micron area for Quantifoil R 2/2 grids) and the precision with which the centers of the holes can be recovered (Figures S5, S6). While the precision with which individual hole centers have been localized in this work is worse than the localization precision of bright fluorescent beads, the large number of holes allows for a reduction in error of the overall projective transformation. Typically, 12 to 16 hole centers are used to register a single field of view. We find that this number of point pairs is sufficient to reduce the registration error below the localization error associated with an individual control point pair. In general, the use of many control point pairs with lower localization precision has proved to be more accurate for registration than a small number of more precise control point pairs.

SI note 2: Manual hole centering method

Initially, algorithmic methods of determining the hole centers were attempted, including centroid estimation with a thresholded image, template matching using an average hole image, and the Hough transformation. However, the most robust results were obtained using the manual method described here. First, we will describe the identification of hole centers in the fluorescence image followed by a comparable process for the identification of holes in the low magnification electron microscopy image.

The fluorescence video is first drift corrected using cross-correlation, and the activation frames are removed. Then the average fluorescence frame is calculated and expanded by a factor of four using bicubic interpolation. The resulting expanded pixels are ~40 x 40 nm. Through a graphical user interface, a user selects two points on a circle to define a hole diameter in the expanded image to be used for the rest of the fluorescence registration. Next, the user selects a region containing a hole and also selects an initial hole center location. The selected region is then viewed on the full screen and the selected hole center overlaid on the grayscale image as a green circle with the previously defined diameter (Figure S4). The user can either accept the hole position or adjust the position by mouse clicking a new center location. In the case that a new center location is chosen, the green circle is updated. The user again assesses the alignment and the process repeats until the hole in the grayscale image and the green circle are well aligned. Once satisfied, the center of the green circle is stored and the next hole in the grayscale average expanded fluorescence image is selected. Typically, 12 to 16 hole centers surrounding a cell of interest are identified.

Following the identification of the hole centers in fluorescence, hole centers are identified by a similar process in the low magnification electron micrograph image. The low magnification micrograph has a field of view of ~15 x 15 μm and contains between 12 and 16 holes. In order to improve the image quality, the low magnification image is first convolved with a uniform 4 x 4 array. Subsequent steps in the hole identification process are the same as for the fluorescence data; a hole diameter is selected followed by a region containing a hole and an initial hole center location. As in the fluorescence case, the hole center is adjusted until there is good agreement between the green circle and the hole in the grayscale image. This step repeated until all holes present in the low magnification electron micrograph have been identified.

Lastly, a coarse alignment using the pattern of cells and grid holes is used to determine the correspondence between holes in the fluorescence and electron micrographs. The result of this process is ~12 to 16 control point pairs that are used for image transformation.

Supporting Media

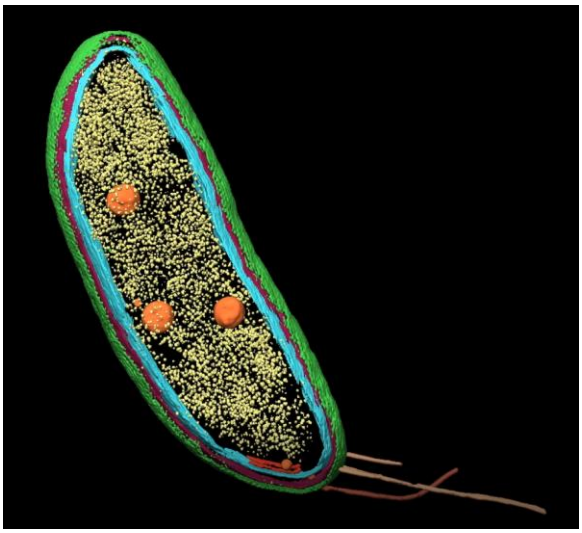

Movie S1: Example CET reconstruction of a wild type *C. crescentus* swarmer cell with a sampling of structures annotated manually with the assistance of a neural network. No fluorescence was used for assignment of structures. (Scale bar: 500 nm)

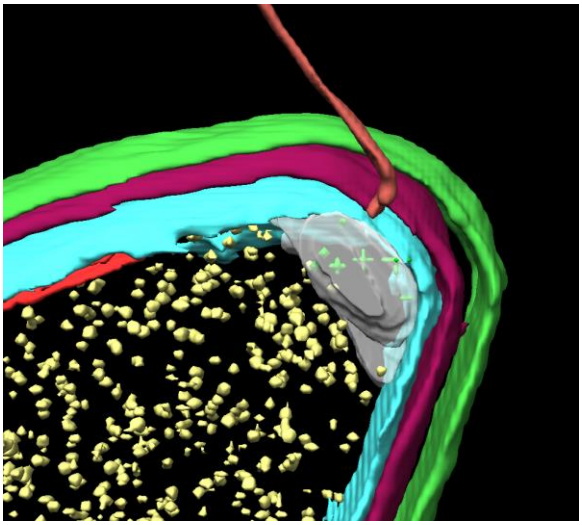

Movie S2: Three-dimensional visualization of PAmKate-PopZ localizations within the context of some traditionally annotated structures, including the ribosome-excluded volume (gray).